Field-Effect Passivation of Undiffused Black Silicon Surfaces

Shaozhou Wang, Xinyuan Wu, Fa-Jun Ma, David Payne, Malcolm Abbott, and Bram Hoex

***Abstract*—Black silicon (b-Si) surfaces typically have a high density of extreme nanofeatures and a significantly large surface area. This makes high-quality surface passivation even more critical for devices such as solar cells with b-Si surfaces. It has been hypothesized that conformal dielectrics with a high fixed charge density (Q_f) are preferred as the nanoscale features of b-Si result in a significant enhancement of field-effect passivation. This article uses 1-D, 2-D, and 3-D numerical simulations to study surface passivation of b-Si, where we particularly focus on the charge carrier control by $|Q_f|$ up to 1×10^{13} cm^{-2} under accumulation conditions. We will show that there is a significant space charge region compression in b-Si nanofeatures, which affects the charge carrier population control for moderate $|Q_f|$ up to $\approx 1 \times 10^{12}$ cm^{-2}. The average surface minority charge carrier density can be reduced by 70% in some cases, resulting in an equivalent reduction in area-normalized surface recombination losses if the effective surface recombination velocity (S_{eff}) is limited by minority carriers. This provides a possible solution for the empirical $S_{\text{eff}} \propto 1/Q_f^4$ reported previously. We will also show that the situation is more complicated for surface passivation films where the ratio between the electron and hole capture cross section (σ_n/σ_p) is higher than 10 for *p*-type surfaces. For commonly used surface passivation films with a $|Q_f|$ larger than $\approx 1 \times 10^{12}$ cm^{-2}, there is little space charge compression for b-Si. Consequently, S_{eff} simply scales with the surface area, i.e., there is no enhanced reduction of surface recombination by field-effect passivation on b-Si.**

***Index Terms*—Black silicon (b-Si), charge carrier population control, field-effect passivation, simulation.**

I. Introduction

LIGHT trapping and surface passivation are two important aspects of surface engineering for high-efficiency solar cells. Black silicon (b-Si) is a textured surface with nanoscale high-aspect-ratio features. These nanofeatures contribute to the advanced light trapping, which can potentially realize high-efficiency b-Si solar cells with near-zero reflectance [1], [2]. However, the surface area of b-Si is significantly larger than that formed by conventional texturing. Thus, a high level of surface passivation is critical for b-Si solar cells [3]. Surface passivation by the industry-standard plasma-enhanced chemical vapor deposited (PECVD) hydrogenated amorphous silicon (a-Si:H) and silicon nitride (SiN_x) could be problematic for b-Si because of the nonconformal deposition resulting from the PECVD process for high-aspect-ratio surface structures [4]. Atomic layer deposition (ALD) is the most promising deposition technique for the surface passivation of the extreme b-Si surfaces since it can achieve a conformal deposition on such structures [5]–[8], and especially ALD Al_2O_3 has been widely studied [2], [5], [6], [9]–[12]. Experimental studies have noted that the passivation provided by ALD Al_2O_3 layers on b-Si surfaces is often better than what would be expected when taking into account the increased surface area. It has been hypothesized that this improved performance by ALD-Al_2O_3 on b-Si is attributed to the enhanced repulsion of minority carriers from the entire nanofeature by a strong interface fixed charge (Q_f), i.e., the field-effect passivation is enhanced on b-Si [10], [13]. By depositing corona charge on the b-Si surface, von Gastrow *et al.* [6] found that the surface recombination velocity (S_{eff}) on b-Si scaled with the inverse of Q_f to the power of four in contrast with planar surfaces where S_{eff} scales with the inverse of Q_f to the power of two. However, it should be noted that it is unlikely that the corona charges can be deposited uniformly on a b-Si surface, which might, at least partly, explain this empirical result [14]. Using 2-D numerical simulations, Turkay *et al.* [15] found that the surface nanofeatures would affect the field-effect passivation and that there could be a field-effect passivation enhancement for lightly doped c-Si under low-injection condition when Q_f magnitude is moderate (5×10^8 cm$^{-2} < |Q_f| < 3 \times 10^{11}$ cm^{-2} for accumulation conditions and 3×10^{10} cm$^{-2} < |Q_f| < 3 \times 10^{11}$ cm^{-2} for inversion conditions). Although these studies have shed some light on the nature of surface passivation of nanofeatures, the detailed mechanism of field-effect passivation on b-Si and its dependence on the nanofeature morphology should be systematically investigated.

From first principles, we know that field-effect passivation relates to Q_f, space charge, band bending, and carrier densities as described in detail by Grove and Fitzgerald [16] and Aberle *et al.* [17]. More recently, Cuevas *et al.* demonstrated that field-effect passivation more generically can be described as a form of charge carrier population control similar to front surface fields by dopant diffusion or band bending resulting from differences in work function. All these approaches result in a change in the charge carrier density, typically resulting

Manuscript received March 2, 2021; revised March 17, 2021; accepted March 20, 2021. Date of publication April 19, 2021; date of current version June 21, 2021. This work was supported by the Australian Renewable Energy Agency under Grant 2017/RND009. *(Corresponding authors: Malcolm Abbott; Bram Hoex.)*

Shaozhou Wang, Xinyuan Wu, Fa-Jun Ma, Malcolm Abbott, and Bram Hoex are with the University of New South Wales, Sydney, NSW 2050, Australia (e-mail: shouzhou.wang@unsw.edu.au; xinyuan.wu@unsw.edu.au; f.ma@unsw.edu.au; m.abbott@unsw.edu.au; b.hoex@unsw.edu.au).

David Payne is with the Macquarie University, Sydney, NSW 2109, Australia (e-mail: david.payne@mq.edu.au).

Color versions of one or more figures in this article are available at https://doi.org/10.1109/JPHOTOV.2021.3069124.

Digital Object Identifier 10.1109/JPHOTOV.2021.3069124

in the concentration of one charge carrier (i.e., the minority carrier) to become significantly lower and thus limiting the surface recombination rate [18]. Recently we reported about charge-assisted carrier population control in 1-D simulations. In that work, we revealed that the space charge regions could be compressed, leading to a significant change in the charge carrier control resulting in a further reduction in the minority charge carrier density. The enhancement of field-effect passivation has been found to strongly depend on both Q_f and the nanofeature diameters [19].

In this work, we will revisit the charge carrier distribution in 1-D and subsequently investigate the charge carrier population control in 2-D and 3-D using Sentaurus TCAD [20]. We will study the surface minority carrier distributions in 2-D and 3-D for Q_f magnitudes from 1×10^9 cm^{-2} to 1×10^{13} cm^{-2} and quantify the impact on the surface recombination rate. Subsequently, we present experimental results that confirm the main findings from the 3-D simulations. Finally, we provide guidance for the optimization of b-Si surface passivation for silicon photovoltaics.

II. Simulation and Experimental Details

A. Model and Parameter Review

This work aims to determine guiding principles for the optimization of the passivation of b-Si surfaces with a particular focus on field-effect passivation using the classic simulation models. The surface recombination model used is the extended Shockley–Read–Hall (SRH) equation for single-energy-level defects [17]

$$U_S = \frac{p_s n_s - n_{ie}^2}{\frac{p_s + p_1}{S_{n0}} + \frac{n_s + n_1}{S_{p0}}} \tag{1}$$

where U_S is the surface recombination rate, n_{ie} is the effective intrinsic carrier density, p_s and n_s are the surface carrier densities, p_1 and n_1 are carrier densities by thermal emission of defects, which are sufficiently small and negligible, and S_{p0} and S_{n0} are the intrinsic surface recombination velocities. As we mainly focus on moderate- and high-level injection conditions in this work, the surface recombination equation can be simplified for the following analysis. Assuming $p_s n_s \gg n_{ie}^2$, $p_s \gg p_1$, and $n_s \gg n_1$, which are generally valid [21], (1) can be simplified as

$$U_S = \frac{p_s n_s}{\frac{p_s}{S_{n0}} + \frac{n_s}{S_{p0}}}\ . \tag{2}$$

The level of surface passivation was quantified by the effective surface recombination velocity S_{eff} defined as

$$S_{\text{eff}} = \frac{U_S}{\Delta n} \tag{3}$$

where Δn is the excess minority carrier density in the bulk at the edge of the space charge region.

A great diversity of passivation materials and relevant stacks has been studied in recent decades. The electrical properties and the corresponding passivation performance not only depend on the material itself, but also heavily rely on the scheme structures, process conditions, and postannealing conditions. The basic principle of field-effect passivation is the charge-assisted population control, hence, the magnitude of fixed charge Q_f at the Si-dielectric interface is our main focus. Table I presents a summary of the typical ranges of Q_f that are reported for the most widely studied silicon surface passivation films, revealing that the magnitude of Q_f is typically in the range of 10^9–10^{13} cm^{-2}.

TABLE I
Summary of the Q_f and σ_n/σ_p Values Reported for Various Surface Passivation Materials

Schemes	Q_f (cm^{-2})	σ_n/σ_p
a-Si:H	$\pm10^9$, $\pm10^{10}$, $\pm10^{11}$ [22]–[24]	-
SiO_x	$+10^{10}$, $+10^{11}$, $+10^{12}$, $+10^{13}$ [17], [25]–[27]	100 – 1000 [17], [28]
SiN_x	$+10^{11}$, $+10^{12}$, $+10^{13}$ [29]–[33]	0.01 – 1* [34]–[36]
SiC_x	$+10^{10}$, $\pm10^{11}$, $+10^{12}$ [37]–[39]	-
AlO_x	-10^{11}, -10^{12}, -10^{13} [40]–[43]	10 – 1000 [42], [44], [45]
AlN_x	$+10^{10}$, -10^{11}, $\pm10^{12}$ [46], [47]	-
TiO_x	$\pm10^{11}$, -10^{12} [48], [49]	-
HfO_x	$\pm10^{11}$, $\pm10^{12}$ [43], [50]–[52]	-
GaO_x	$\pm10^{11}$, $\pm10^{12}$ [53]–[55]	-
MgO_x	$\pm10^{10}$, $\pm10^{11}$ [56]	-
PO_x	$+10^{12}$ [57], [58]	-
TaO_x	-10^{12} [59], [60]	-
NbO_x	-10^{12} [61]	-
ZrO_x	-10^{10} [62]	-

*Ratio of the dominant defect.

However, the extended SRH model (1) governs that the intrinsic recombination velocity ratio of electron and hole (S_{n0}/S_{p0}), which relates to the ratio of the electron and hole capture cross section (σ_n/σ_p), is also critical for quantifying the surface recombination rate. The surface recombination rate is highest when $p_s/n_s \approx \sigma_n/\sigma_p$ [17], and is limited by either the electron concentration (when $n_s/\sigma_p < p_s/\sigma_n$) or hole concentration (when $n_s/\sigma_p > p_s/\sigma_n$). Furthermore, combining with (2) and acknowledging that $S_{n0} = v_{thn}\ N_{it}\sigma_n$ and $S_{p0} = v_{thp}\ N_{it}\sigma_p$, (3) can be simplified under *p*-type accumulation condition

$$S_{\text{eff}} = \left(\frac{N_{it}}{\Delta n}\right)\ \frac{p_s n_s}{\frac{p_s}{v_{thn}\sigma_n} + \frac{n_s}{v_{thp}\sigma_p}} \approx \frac{N_{it} v_{thn} \sigma_n n_s}{\Delta n} \tag{4}$$

where v_{thn} and v_{thp} are the thermal velocities of electrons and holes, and N_{it} is the energy-independent interface defect density, which relates to chemical passivation. Equation (4) reveals that the surface recombination only depends on the surface minority carrier concentration when the majority-carrier-related term can be neglected. As the asymmetry of v_{thn} and v_{thp} is small ($v_{thn}/v_{thp} \approx 1.2$), this condition will be satisfied only when $p_s/\sigma_n >> n_s/\sigma_p$. Since the asymmetry of surface carrier densities is typically larger than that of the surface capture cross section, $p_s >> n_s$ should be satisfied primarily, which is generally realized when Q_f is effectively high.

TABLE II
SUMMARY OF WAFER DIAMETERS, PHYSICS MODELS, AND PARAMETERS USED IN THE SIMULATIONS

Basic setup	
Silicon bulk thickness	200 µm
Dielectric layer thickness	20 nm
Bulk doping	Boron 5×10^{15} cm^{-3}
Temperature	298 K
Injection condition	Quasi-steady-state conditions with a uniform generation
Carrier statistics	Fermi–Dirac statistics and statistic quantum correction by the basic density gradient quantization model [66]
Bulk setup	
Recombination	Richter's Auger recombination model [67], radiative recombination model, and single-level-defect Shockley-Read-Hall (SRH) recombination model [68]
SRH carrier lifetime	$\tau_{n0} = \tau_{p0} = 2\times10^{-3}$ s
Band gap narrowing	Schenk's model [69]
Mobility	Philips unified mobility model [70]
Space charge distribution	Poisson' equation [16]
Surface setup	
Surface recombination rate U_S	Extended SRH equation for single-level defects
Interface fixed charge Q_f	From -1×10^{9} to -1×10^{13} cm^{-2}
Local intrinsic surface recombination velocity S_0*	$S_{n0} = 0.1 \times S_{p0} = 3000$ cm s^{-1} $S_{n0} = 10 \times S_{p0} = 3000$ cm s^{-1} $S_{n0} = 100 \times S_{p0} = 3000$ cm s^{-1}

*Assuming the thermal velocities of electrons and holes are identical ($v_{thn} = v_{thp}$), therefore $S_{n0}/S_{p0} = \sigma_n/\sigma_p$.

Since the σ_n/σ_p values have not been reported for all surface passivation films, we will predominantly focus on the σ_n/σ_p ranges, which are reported in Table I for the most widely studied surface passivation films. The σ_n/σ_p range of AlO_x is similar to that of SiO_x, very likely because of the presence of a thin SiO_x at the AlO_x–Si interface [44], [63]. It is not unrealistic to assume that the σ_n/σ_p of other oxide passivation layers would have a similar thin interfacial SiO_x and consequently a similar σ_n/σ_p ratio. In this work, we will examine the following three σ_n/σ_p ratios.

1) $\sigma_n/\sigma_p = 0.1$, which represents the condition of $\sigma_n < \sigma_p$ observed at SiN_x–Si interfaces.
2) $\sigma_n/\sigma_p = 10$, which represents the condition of $\sigma_n > \sigma_p$ observed at oxide–Si interfaces.
3) $\sigma_n/\sigma_p = 100$, which represents the condition of $\sigma_n >> \sigma_p$ also observed at oxide–Si interfaces.

B. Simulation Setup

The numerical simulation work was conducted by means of multidimensional models using Sentaurus TCAD [20], [64], [65]. The simulations focused on *p*-type silicon with negative Q_f values (in cm^{-2}), i.e., we focused on accumulation conditions. The injection level was determined by the excess minority carrier density at the edge of the space charge region. The details of the simulation setup in this work are summarized in Table II, and a simplified determination procedure of surface passivation

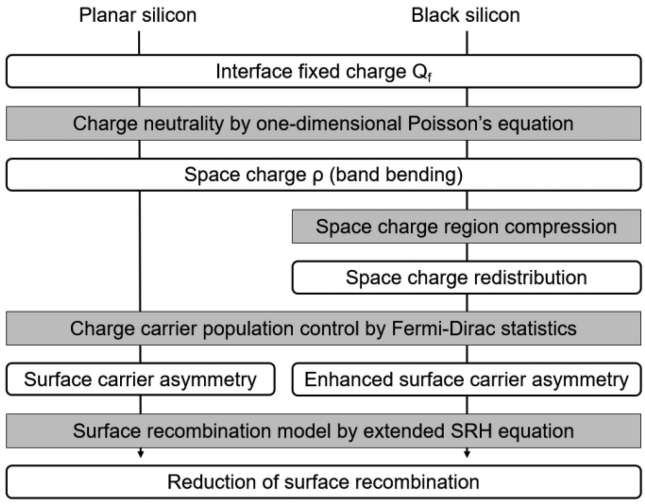

Fig. 1. Simplified schematic diagram of a procedure for the determination of field-effect passivation on planar silicon and b-Si.

performance is shown in Fig. 1. The space charge and minority carrier density in 1-D were determined by a simple two-parallel-surface model. The minority carrier distribution and local surface recombination in the nanofeature were modeled in 2-D, and the b-Si surface recombination was modeled in 3-D numerically for both b-Si wafers and planar wafers. The unit cell representing the b-Si wafer was modeled by using a rotationally symmetric 2-D structure, as shown in Fig. 2, which resulted in a cone-like feature. To unambiguously determine the influence of the nanofeature on the surface passivation compared with a planar surface, we define two factors that associate the absolute effective surface recombination velocities of b-Si ($S_{\text{eff BS}}$) and the reference planar surface ($S_{\text{eff planar}}$): 1) the area factor F_{area}, which is the ratio of total surface area and projected area; 2) the S_{eff} improvement factor F_{SRV}, which is defined as

$$F_{SRV} = \frac{S_{\text{eff BS}}/F_{\text{area}}}{S_{\text{eff planar}}} \tag{5}$$

where $S_{\text{eff BS}}/F_{\text{area}}$ is the area-normalized S_{eff} of the b-Si surface. An F_{SRV} value of 1 means that the surface recombination on b-Si simply scales with the surface area, whereas an F_{SRV} lower than 1 implies that the surface recombination is less than you would expect from the increase in surface area.

For a more comprehensive investigation on the characteristics of b-Si surface passivation, a more sophisticated optical simulation method would be required such as finite-difference time domain to quantify the spatially resolved electron-hole pair generation rate. It is shown by Rahman and Boden [71] that the injection levels can be very nonuniform for b-Si surfaces, some parts of which having $\Delta n >> 1 \times 10^{15}$ cm^{-3}. However, as we wanted to focus on the perturbation of charge-carrier control by b-Si nanofeatures, we decided to assume a uniform optical generation rate in this work as well as a constant bulk injection level of $\Delta n = 1 \times 10^{15}$ cm^{-3}. As this injection level is well below the bulk doping level, it is not expected to change the band bending close to the surface significantly [17].

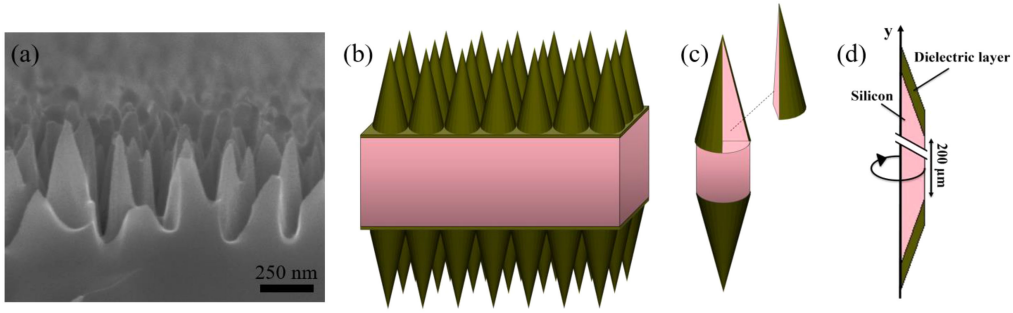

Fig. 2. (a) SEM image of RIE b-Si used in experiments and the schematic of (b) the ideal b-Si wafer model, (c) the unit cell of the ideal b-Si wafer model, and (d) the 2D-to-3D structure of the unit cell by cylindrical coordinate for the numerical simulation. The dielectric layer thickness was 20 nm and the unit cell bulk thickness was 200 μm.

C. Experimental Details

The experiments were performed on double-side polished, 500 μm thick, boron-doped Czochralski silicon wafers with <100> crystal orientation and a resistivity of 5–6 Ω·cm. A b-Si surface texture with an average height of ≈300 nm and an average diameter of ≈150 nm was formed on a single side of these polished samples using reactive ion etching (RIE) with an STS DRIE Pegasus tool. The samples were etched in an SF_6 (70 sccm) and O_2 (100 sccm) plasma for 6 min at a coil power of 3 kW. Before the dielectric layer deposition, the b-Si samples and reference planar samples received a standard Radio Corporation of America cleaning process. A ≈22 nm ALD Al_2O_3 dielectric layer was deposited on both sides of the samples using a CNT Savannah S200 tool with trimethyl aluminum as the precursor and H_2O as the oxidant at a substrate temperature of 200 °C. The surface passivation provided by the dielectric layers was activated by rapid thermal annealing using a Semco RTP-Jetfirst 200 tool with two different recipes: 400 °C for 10 min (Group 1) and 350 °C for 1 min (Group 2) in order to achieve different Q_f values in the films [72]. Topographical characterization in this work was performed by a field-emission scanning electron microscope (SEM) using an FEI Nova NanoSEM 450 system. The τ_{eff} was measured by quasi-steady-state photoconductance decay method using a Sinton WCT-120 tool with the polished side facing up in order to ensure an equal generation rate in both samples. The Al_2O_3–Si interface total charge density Q_{tot} and defect density D_{it} of the polished surfaces were determined by corona oxide characterization of semiconductors [73] using a Semilab SDI PV2000 tool.

III. Results and Discussion

A. Minority Carrier Distribution in 1-D Simulations

In this section, we will discuss the main findings from our earlier work about the charge carrier population control resulting from space charge compression in 1-D, which is relevant for understanding the results in 2-D and 3-D. Space charge ρ induced in the near-surface region is the mirrored charge of Q_f because of the nature of charge neutrality. We define the effective relative charge ω to evaluate the proportion of nonmirrored charge at a certain depth for an infinite-thick substrate. It is defined as

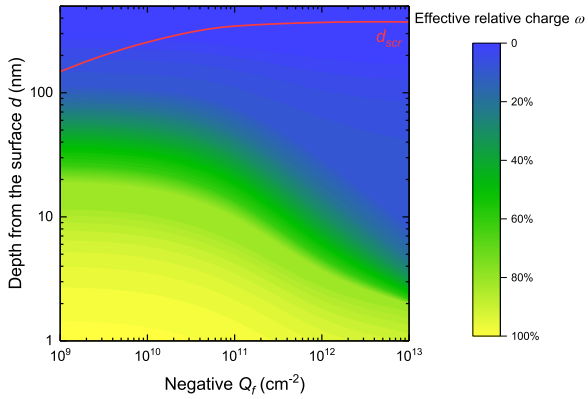

Fig. 3. Effective relative charge ω as a function of negative Q_f and depth from the surface d of the planar silicon under an injection level of 1×10^{15} cm^{-3}. ω indicates the fraction of nonmirrored Q_f at a certain depth d. Since the space charge ρ has an opposite polarity to Q_f , ω is 100% at the surface and reduced as d increases, and will be ≈0 at the edge of space charge region d_{scr}. The red line shows d_{scr} as a function of negative Q_f. d_{scr} is defined at the depth where $\rho = 1 \times 10^{13}$ cm^{-3} ($\rho << N_A + \Delta n$). The result is reproduced from [19].

$$\omega = \frac{Q_f + \int_0^d \rho(x)\,dx}{Q_f} \tag{6}$$

where d is the investigated depth and $\rho(x)$ is the space charge density at depth x. When $d = 0$, $\omega = 100\%$. When d is equal to the depth of the space charge region, $\omega = 0$. Fig. 3 shows the relative distribution of ρ resulting from Q_f at the surface. When $|Q_f| < 1 \times 10^{11}$ cm^{-2}, ρ extends very deep into the wafer and $\omega \approx 80\%$ at 10 nm, meaning that 80% of charge is nonmirrored at this depth. However, when Q_f is relatively large ($|Q_f| > 1 \times 10^{12}$ cm^{-2}), ρ is mainly concentrated in the near-surface region. $> 80\%$ of ρ is already mirrored in the first 10 nm ($\omega < 20\%$) and there is ≈50% of ρ already mirrored in the first 3 nm ($\omega = 50\%$) for a $Q_f = -1 \times 10^{13}$ cm^{-2}. Therefore, the first finding is that Q_f is almost fully mirrored at 100 nm from the surface for all relevant Q_f values and is mirrored increasingly closer to the surface for higher Q_f values. In Fig. 4, we demonstrate the impact on the ρ distribution when the wafer thickness is smaller than the depth of the space charge region. We simulate the impact by the addition of second surface

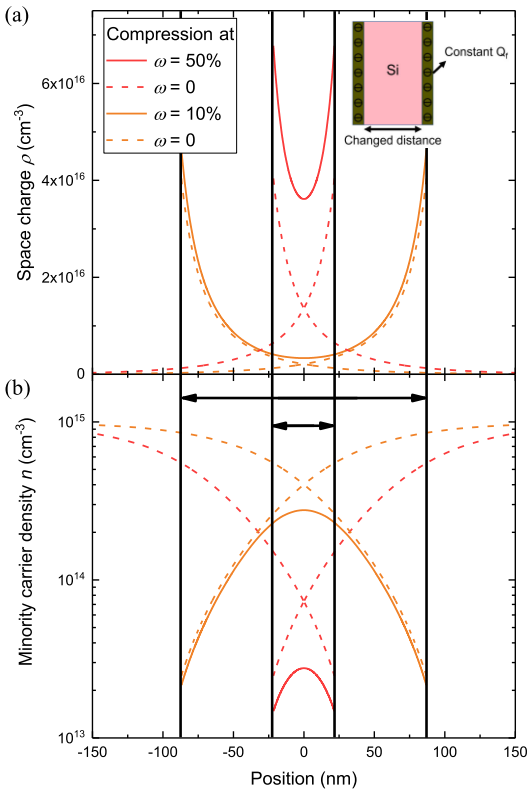

Fig. 4. (a) Space charge density ρ and (b) minority carrier density as a function of the position in two symmetrically lifetime structures. The position is shown relative to the middle of the sample for easy comparison. The thickness of the two lifetime structures (indicated by the black arrows) was chosen such that 50% (red) or 90% (yellow) or the charge was already mirrored at the depth of the second surface. The solid lines show the values for the symmetrical structures, whereas the dashed lines show the values for each surface without the effect of the second surface. The results clearly show compression of the space charge and corresponding reduction in the minority carrier density at the surface. The result is reproduced from [19].

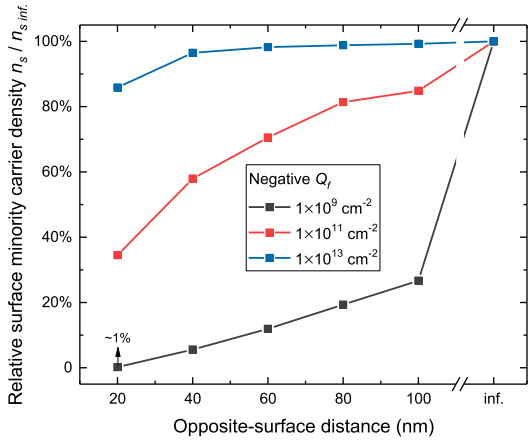

Fig. 5. Effects of opposite-surface distance on the surface minority carrier densities for different Q_f in 1-D simulations. The surface minority carrier densities are compared with the densities in the substrate with an infinite thickness to evaluate the effectiveness (relative surface minority carrier density in percentage).

with an identical Q_f in a similar way as would happen for a typical symmetrically coated minority charge carrier lifetime sample that is used for experimentally determining S_{eff}. We reduce the distances of opposite surfaces of wafers to two conditions: 1) 43 nm opposite-surface distance where 50% of ρ is redistributed; 2) 174 nm opposite-surface distance where 10% of ρ is redistributed. We show that this results in space charge region compression and a corresponding change in the minority carrier density. As the model is symmetric and the net electric field is zero at the center, the compressed space charge region depth is half of the opposite-surface distance. The impact strongly depends on the original ω at that position. When there is 50% of ρ redistributed (compression starts at the position where $\omega = 50\%$ originally), we see a remarkable difference in ρ and the resulting minority carrier charge density. When there is only 10% of ρ redistributed, the impact on ρ is relatively small and, consequently, the minority carrier concentration at the surface is barely affected [19].

Consequently, we can conclude that space charge region compression is determined by the original ω value at the center of opposite surfaces. There will be a significant ρ increase when ω is relatively high, whereas for small ω values, there will be no impact. As we are focussing on accumulation conditions, space charge region compression will always result in a reduction of the minority carrier density at the surface. In Fig. 5, we show the relative surface minority carrier density as a function of the distance between the opposite surfaces for three Q_f values. When the Q_f value is high, we can only see a marginal impact on the relative surface minority carrier density with only a ≈15% reduction for a distance of 20 nm, which can be attributed to the fact the ρ is mainly concentrated at the first 5 nm from the surface. For moderate Q_f value of -1×10^{11} cm^{-2}, the relative surface minority carrier density is decreased from ≈83% with a 100 nm distance, to ≈35% with a 20 nm distance. Under the low Q_f value of -1×10^{9} cm^{-2}, the effects of the decreasing opposite-surface distance are the most remarkable. There is ≈75% reduction of the relative surface minority carrier density with a 100 nm distance, and the reduction can be even up to ≈99% when the opposite surfaces are only 20 nm apart.

B. Minority Carrier Distribution in 2-D Simulations

Next, we will investigate the minority carrier distribution in 2-D nanofeatures and compare them to planar surfaces.

Fig. 6(a)–(c) shows the minority carrier distribution in the 2-D nanofeatures with a width of 100 nm and a height of 500 nm relative to planar surfaces. When Q_f is low, the nanofeature can enhance the carrier asymmetry and reduce the minority carrier density n, as illustrated in Fig. 6(a). For a moderate $Q_f = -1 \times 10^{11}$ cm^{-2} shown in Fig. 6(b), it can be seen that there is a reduction of n up to 90% in the nanofeature compared with the planar surface, especially near the nanofeature peak. In Fig. 6(c), there is almost no difference for n of the nanofeature compared with the planar surface. This means that the nanofeature will hardly affect the charge carrier population control when Q_f is high. Fig. 6(d) shows the relative surface minority carrier density of nanofeatures ($n_{s\ \text{BS}}/n_{s\ \text{planar}}$). It indicates that the nanofeature leads to a relatively uniform ≈35% to ≈45% reduction of n_s for a low Q_f (-1×10^{9} cm^{-2}). When the Q_f value is moderate at -1×10^{11} cm^{-2}, the n_s is decreased to $< 40\%$ except for the region near the bottom of nanofeature, whereas

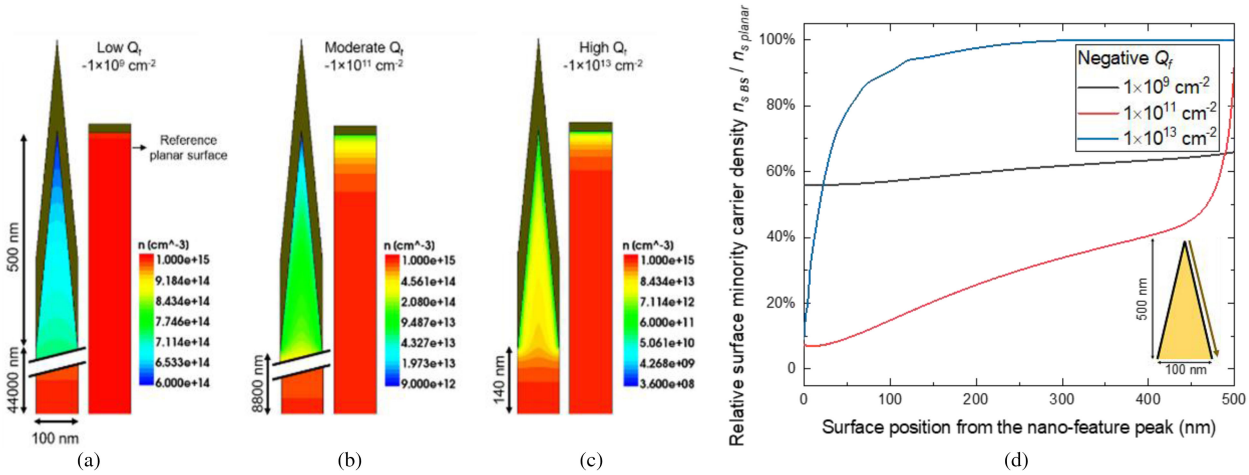

Fig. 6. Minority carrier distributions under (a) low, (b) moderate, and (c) high Q_f conditions with 1×10^{15} cm^{-3} injection in the nanofeatures compared with a planar surface, and (d) the relative surface minority carrier density at the nanofeature surfaces from the peak to the bottom. The simulation setup is shown in Table II. The simulated feature had a width of 100 nm and a height of 500 nm.

the significant reduction in n_s is concentrated in the peak of nanofeature for the high Q_f value at -1×10^{13} cm^{-2}. In general, we can see some consistency as well as inconsistency between the 1-D results in Fig. 5 and 2-D results in Fig. 6. Both results of high Q_f show a near 100% of relative surface minority carrier density, except when the opposite-surface distance is extremely small. However, when comparing the low and moderate Q_f conditions, the relative surface minority carrier density of low Q_f is lower in 1-D, whereas its 2-D result is higher. This can be explained by the effect of dimension expansion where the minority carriers will be repelled into a deep region in 2-D. It should be noted that the carrier concentration is affected up to depths of 44 and 8.8 μm, respectively, for low and moderate Q_f. This is not the results of space charge compression but from a relatively high surface recombination rate. For example, the surface recombination current for a 500 nm height nanofeature with $Q_f = -1 \times 10^9$ cm^{-2} is 3598 fA cm^{-2}, extremely large compared with the bulk recombination current of only 20 fA cm^{-2}. As we are simulating steady-state conditions, the cumulative recombination rate has to equal the cumulative generation rate. The high surface recombination current results in a high minority carrier diffusion current to the surface, and the magnitude of the diffusion current depends on the nanofeature size (as the area factor F_{area} increases as a function of the nanofeature size), i.e., the minority carrier profile in the sample is the result of a diffusion current and not the result of charge carrier population control from the surface Q_f. This work predominantly focuses on the minority carrier density at the surface, which is, in most cases, not materially affected by the diffusion current.

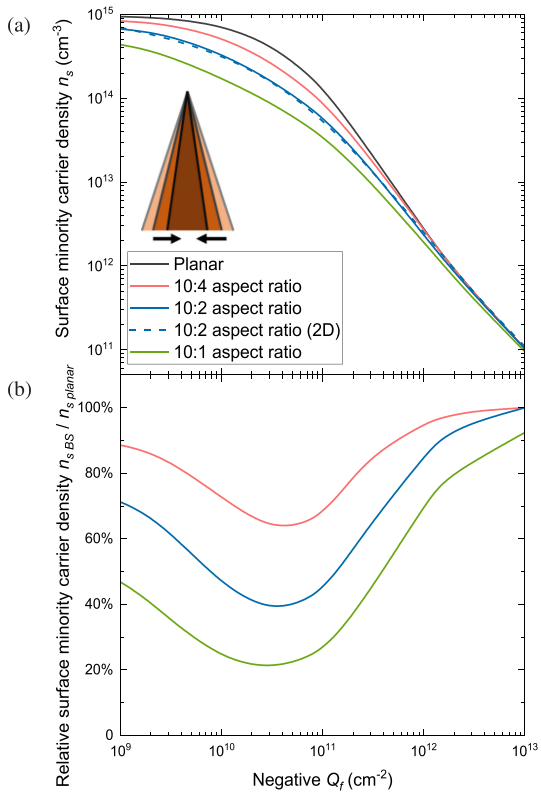

Fig. 7. 3-D comparison of (a) the average surface minority carrier density of planar and b-Si surfaces and (b) the corresponding relative surface minority carrier density with 500 nm height and different aspect ratios under 1×10^{15} cm^{-3} injection condition. The simulation setup is shown in Table II.

C. Surface Minority Carrier Density in 3-D Simulations

In the previous sections, we revealed the mirror ρ distribution characteristics and examined the minority carrier distribution in nanofeatures by 1-D and 2-D simulations, especially the surface minority carrier. In this section, we will still focus on the surface minority carrier and expand the simulations to 3-D.

Fig. 7(a) presents the effects of the nanofeature aspect ratio on surface minority carrier density n_s under different Q_f conditions. For a 10:2 aspect ratio, the 2-D and 3-D results are compared and show a nonsignificant difference. This means the findings by 2-D simulations can be extrapolated for 3-D. In Fig. 7(b), the 3-D results demonstrate that the relative surface

minority carrier density is effectively reduced in the moderate Q_f range and the reduction is enlarged as the nanofeature aspect ratio increases, because of the reduction mainly depending on the distance between the surfaces. In the investigated highest aspect ratio, the surface minority carrier density can be reduced to 20%, and it can be expected that the reduction can be $> 80\%$ when the aspect ratio is larger than 10:1. However, as a result of a deeper influenced region, the nanofeature with low Q_f values has a higher relative surface minority carrier density. In addition, the surface minority carriers of nanofeature with high Q_f values are hardly affected, and this can be explained by the fact that the charge carrier population, in this case, is not significantly affected by nanofeature diameters > 10 nm.

D. Effects of σ_n/σ_p and Injection Levels on Surface Passivation

We have investigated the relative surface minority carrier densities of nanofeatures by 1-D, 2-D, and 3-D simulations. However, the relative surface minority carrier can be used to evaluate the surface passivation performance only when $n_s/\sigma_p << p_s/\sigma_n$ as discussed in Section II-A. Here, we will go further to determine the effects of σ_n/σ_p and injection levels on the surface passivation of a nanofeature by 2-D simulations. The surface passivation performance is evaluated by the S_{eff} improvement factor F_{SRV} calculated by (5).

Fig. 8 presents the corresponding surface passivation performances of cases in Fig. 6 for three different σ_n/σ_p and two injection levels for a nanofeature with a width of 100 nm and a height of 500 nm. For the moderate (-1×10^{11} cm^{-2}) and high (-1×10^{13} cm^{-2}) Q_f, the graphs are mostly identical to the relative minority carrier density graphs shown in Fig. 6(d) for an identical nanofeature, in particular for all conditions shown with $\sigma_n/\sigma_p = 0.1$. This is because of the fact that surface recombination is limited by the supply of minority carriers and can be described by (4). For low Q_f (-1×10^{9} cm^{-2}), the value of F_{SRV} is higher than that of relative minority carrier density as surface recombination in this case also is determined by the majority carrier density. The situation gets a bit more complicated when the σ_n/σ_p is 10 or 100. For low injection levels, surface recombination is still mainly limited by the surface minority carrier density. For an injection level of 1×10^{15} cm^{-3}, however, surface recombination has a strong dependence on the supply of both electrons and holes and field-effect passivation can, in some cases, even increase surface recombination losses. This phenomenon has been well discussed in the work of Aberle *et al.* [17], where it was presented that there is a maximum S_{eff} when $p_s/n_s \approx \sigma_n/\sigma_p$, which is valid for both of accumulation and inversion conditions. This maximum S_{eff} was also observed in previous work [18], [42], [74]. Here, assuming $\sigma_n/\sigma_p = S_{n0}/S_{p0} = 100$ under 1×10^{15} cm^{-3} injection, we find that the maximum S_{eff} at $Q_f \approx 5 \times 10^{10}$ cm^{-2} in 1-D planar condition. When $Q_f = 1 \times 10^{9}$ cm^{-2} on the nanofeature surface, compared with the planar surface, the equivalent surface carrier densities will be approaching the condition where $Q_f \approx 5 \times 10^{10}$ cm^{-2} on the planar surface. This phenomenon is not only of academic interest as a 1×10^{15} cm^{-3} injection level is quite typical for solar cell operations. Consequently, enhanced charge carrier population control will not always contribute to the reduction of surface recombination losses. An improvement in surface passivation performance can always be achieved only when σ_n is not much larger than σ_p for *p*-type accumulation conditions, and vice versa for *n*-type accumulation conditions.

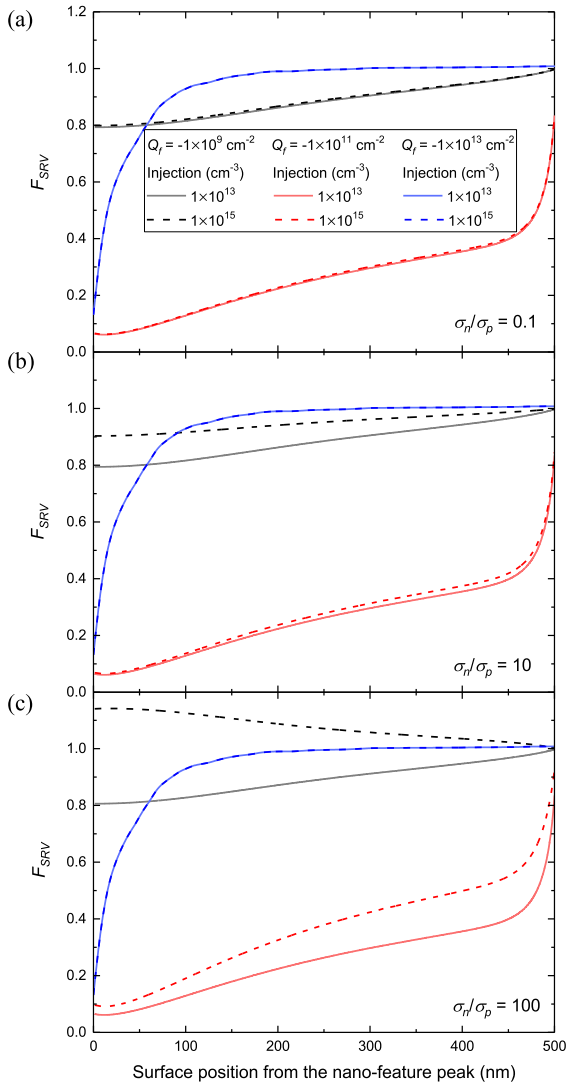

Fig. 8. Effects of σ_n/σ_p, Q_f, and injection levels on the surface passivation performance for a nanofeature with a width of 100 nm and a height of 500 nm (identical case in Fig. 6). Three σ_n/σ_p ratios are shown: (a) 0.1, (b) 10, and (c) 100. For each σ_n/σ_p ratio, three different Q_f and two different injection levels are applied. The change of surface passivation performance is evaluated by F_{SRV}. A lower F_{SRV} means a better surface passivation compared with a planar surface.

E. Surface Passivation Under a High σ_n/σ_p Condition in 3-D Simulations and Experiments

In this section, we will focus on the improvement of surface passivation performance under a 1×10^{15} cm^{-3} injection with a high $\sigma_n/\sigma_p = 100$ (i.e., $S_{n0}/S_{p0} = 100$), which is widely observed in oxide surface passivation films. This section includes defining Q_f ranges based on F_{SRV} and investigating the effects of the b-Si nanofeature diameter, size, and height on the

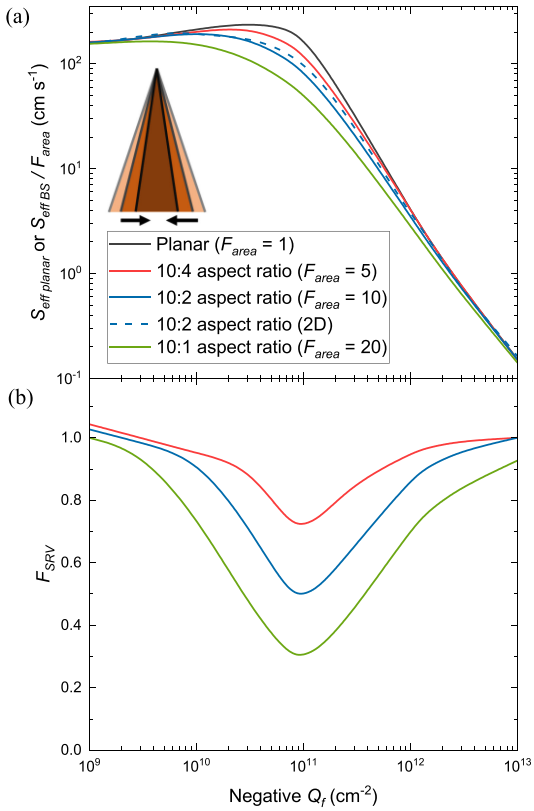

Fig. 9. Corresponding (a) effective surface recombination velocities of reference planar surface and area-normalized b-Si and (b) F_{SRV} of cases in Fig. 7 under $S_{n0} = 100 \times S_{p0} = 3000$ cm s^{-1} ($\sigma_n/\sigma_p = 100$) and 1×10^{15} cm^{-3} injection condition. The absolute $S_{\text{eff BS}}$ can be determined accordingly.

field-effect passivation under different Q_f conditions. Finally, the findings will be validated by experiment results.

Fig. 9 shows the corresponding area-normalized S_{eff} and F_{SRV} of Fig. 7 to quantify the change of surface passivation performance. We can see a very similar trend of the relative surface minority carrier densities in Fig. 7(b) and F_{SRV} in Fig. 9(b) when $|Q_f| > 1 \times 10^{11}$ cm^{-2}. This is attributed to the fact that the surface recombination is only decided by the surface minority carrier density when Q_f is moderate or high. Hence, the reduction of surface minority carrier density will contribute to the reduction of F_{SRV} directly. However, when $|Q_f| < 1 \times 10^{11}$ cm^{-2}, the surface passivation will also be limited by the supply of majority carriers, and there is even inferior surface passivation under low Q_f conditions as discussed in Section III-D. According to Fig. 9(b), we can define the Q_f range by low ($|Q_f| < 1 \times 10^{10}$ cm^{-2}), moderate (1×10^{10} cm^{-2} $< |Q_f| < 1 \times 10^{12}$ cm^{-2}), and high ($|Q_f| > 1 \times 10^{12}$ cm^{-2}).

The effects of the b-Si nanofeature sizes and heights are investigated by three surface passivation schemes with widely observed Q_f (-1×10^{11} cm^{-2}, -1×10^{12} cm^{-2}, and -3×10^{12} cm^{-2}) and constants S_{n0} and S_{p0}, as shown in Figs. 10 and 11. The simulations investigate the b-Si with diameters from 60 to 180 nm, and heights from 100 to 500 nm ($F_{\text{area}} = 2 - 10$), which are practical for most RIE fabricated b-Si surfaces [3]. Fig. 10 shows that increasing the nanofeature size will lead to the enlargement of F_{SRV}. Specifically, the area-normalized S_{eff}

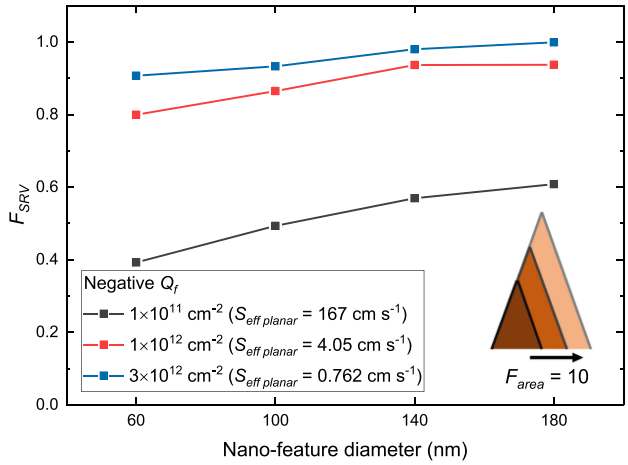

Fig. 10. Effects of nanofeature sizes on F_{SRV} with the constant aspect ratio 10:2 (area factor $F_{\text{area}} = 10$). Three different Q_f are investigated under $S_{n0} = 100 \times S_{p0} = 3000$ cm s^{-1} and 1×10^{15} cm^{-3} injection condition. The absolute $S_{\text{eff BS}}$ can be determined by (5).

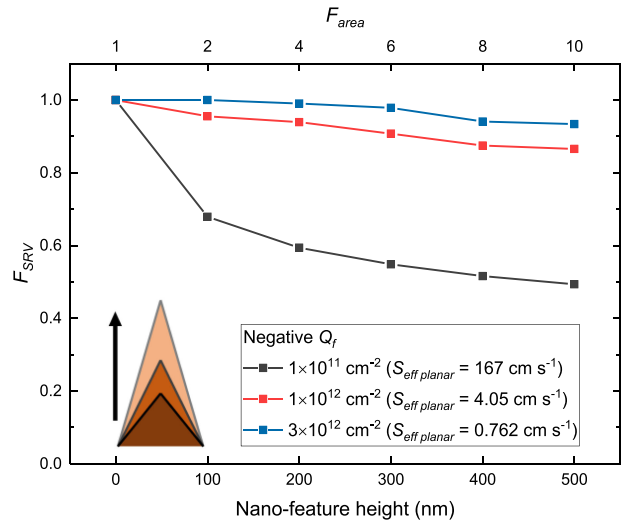

Fig. 11. Effects of nanofeature heights on F_{SRV} by the constant feature diameter 100 nm. Three different Q_f are investigated under $S_{n0} = 100 \times S_{p0} = 3000$ cm s^{-1} and 1×10^{15} cm^{-3} injection condition. The absolute $S_{\text{eff BS}}$ can be determined by (5).

reduction is relatively significant under moderate Q_f conditions (-1×10^{11} cm^{-2}) and its F_{SRV} value is in the range of 0.4 – 0.6. Nevertheless, for high Q_f values, the area-normalized S_{eff} reduction is relatively modest ($F_{SRV} > 0.8$), which is consistent with the previous conclusions. Fig. 11 indicates that increasing the nanofeature height will contribute to the reduction of F_{SRV}. The nanofeature with moderate Q_f has a $F_{SRV} = 0.5 - 0.7$, whereas the high Q_f will only lead to $F_{SRV} > 0.9$. It should be noted that there is a significant area-normalized S_{eff} reduction from the planar surface to the short nanofeature (from 0 to 100 nm height) with $F_{SRV} \approx 0.7$ for $Q_f = -1 \times 10^{11}$ cm^{-2}. This means even a slight b-Si texturing can cause a remarkable reduction of surface recombination losses for moderate Q_f.

The results of Figs. 10 and 11 can be understood by the findings from Sections III-A and III-B. For high negative Q_f

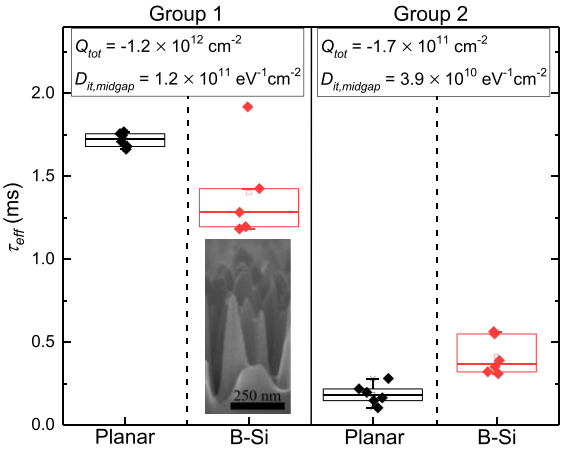

Fig. 12. Measured τ_{eff} of Groups 1 and 2 at injection 3×10^{15} cm^{-3}. The interface properties shown were determined on planar samples.

of -3×10^{12} cm^{-2}, the space charge is mirrored close to the surface and consequently there is no improvement in field-effect passivation by space charge compression with a F_{SRV} value of 1 irrespective of the shape of the nanofeature. For lower negative Q_f, the F_{SRV} is lower than 1 indicating a relative improvement in surface passivation and the value reduces for smaller features because of space charge compression. In addition, Figs. 10 and 11 compare three Q_f cases where there is either moderate or strong field-effect passivation with constant chemical passivation, which leads to large differences in $S_{\text{eff planar}}$. The main focus of this work is on the relative surface recombination compared with the projected area as expressed by F_{SRV}. The absolute $S_{\text{eff BS}}$ can easily be calculated from (5).

We empirically validate the findings by comparing the change of surface passivation performance for a moderate Q_f case and a high Q_f case. We propose reasonable assumptions for the experimental results shown in Fig. 12, to focus on the effects of b-Si nanofeatures on the surface carrier densities within the scope of this work. The D_{it} and Q_{tot} of each group were only measured on planar samples. It is assumed that the measured lowest D_{it} is $D_{it,midgap}$; $Q_{\text{tot}} = Q_f$ as $D_{it,midgap}$ is relatively small; the effects of surface damage and crystal orientations on b-Si surfaces are negligible; the surface passivation layers on b-Si surfaces are conformal and identical to those on planar surfaces; the sole factor that causes the variation of τ_{eff} is the surface passivation. The experimental results validate that there is a beneficial surface carrier population control enhancement (field-effect passivation enhancement) when Q_f is moderate. Since Q_f was high in Group 1, the surface passivation on the b-Si samples was inferior compared with the reference planar samples because of the larger surface area and the modest field-effect passivation enhancement. However, when Q_f was moderate as resulted in Group 2, the surface recombination losses on the b-Si samples had a clear reduction caused by the field-effect enhancement, which even compensated for the increase in surface area as the b-Si τ_{eff} was higher than the planar τ_{eff}. Therefore, instead of the field-effect passivation enhancement, which was proposed in the literature, the excellent surface passivation of the high-Q_f ALD-Al_2O_3 layers on b-Si surfaces can be attributed to the extremely low S_{eff} [40], [67], [75], [76], and consequently, the total recombination in the solar cell is not dominated by surface recombination despite the larger surface area.

F. Suggestions for Black Silicon Surface Passivation Optimization

Table I suggests that most surface passivation schemes will show a moderate or high Q_f, except a-Si:H and some less common novel passivation schemes. This means there is no universal solution to the b-Si surface passivation optimization for a given passivation material. According to the conclusions of Sections III-D and III-E, assuming the passivation layer coverage is conformal on the b-Si surface, decreasing the b-Si surface area will reduce surface recombination losses as the number of surface defects scales with the surface area. For passivation films with a low Q_f at an injection level of 1×10^{15} cm^{-3}, the effects of nanofeatures on the surface passivation depend on σ_n/σ_p, which is determined by the passivation film. For films with a σ_n/σ_p above 10, we can see an increase in surface recombination losses when using surface passivation films with a low Q_f. For surface passivation films with a moderate Q_f, balancing the surface area and the nanofeature structure is important, since both increasing the aspect ratio and decreasing the size can enhance the field-effect passivation effectively but also change the surface area. According to Section III-E, the typical RIE fabricated b-Si surfaces with moderate Q_f will show a $F_{SRV} = 0.3$–0.7. This means the issue of increased surface areas with $F_{\text{area}} = 1.4$–3.3 for such b-Si surfaces could be eliminated by moderate Q_f because of the compensation of enhanced field-effect passivation. Finally, although there is no additional reduction in surface recombination for b-Si surfaces compared with planar surfaces when using passivation films with a high Q_f, obviously these films still provide the best surface passivation on these surfaces.

In this work, we only focused on accumulation conditions, but the conclusions also guide the surface passivation under inversion conditions. For optimal surface passivation, a relatively high Q_f is required to invert the surface. However, because of the effects of enhanced charge carrier population control in the nanofeatures, the required magnitude of Q_f will be lower on b-Si compared with planar surfaces. One representative case is thermally grown SiO_2 on *p*-type substrates. Khandelwal *et al.* [77] found that the surface passivation of the undiffused *p*-type b-Si surface by thermally grown SiO_2 is better than that of the reference random-pyramid surface, whereas the b-Si area was beyond twice of the random-pyramid area. Thermally grown SiO_2 typically shows a moderate positive Q_f [17], which may not be able to cause a beneficial inversion depending on the surface doping. However, in this case, it is possible that the inversion is beneficial and the improved field-effect passivation of the b-Si sample overcomes the drawback of its larger surface area.

IV. Conclusion

The characteristics of field-effect passivation on undiffused b-Si surfaces under accumulation conditions have been investigated through 1-D/2-D/3-D wafer modeling using Sentaurus TCAD. The effects of b-Si nanofeatures on the charge carrier population control for the surface passivation have been studied. It is shown that the minority charge carrier concentration can be significantly lower on b-Si compared with a planar surface. This possibly explains why a $1/Q_f^4$ dependence was reported in [6]. By examining the surface carrier population control of the b-Si nanofeatures and extracting the corresponding area-normalized S_{eff}, we find low Q_f conditions ($|Q_f| < 1 \times 10^{10}$ cm^{-2}) will lead to an improved or inferior field-effect passivation depending on σ_n/σ_p and injection levels. When Q_f is in the moderate range (1×10^{10} cm$^{-2} < |Q_f| < 1 \times 10^{12}$ cm^{-2}), there is a remarkable reduction of the area-normalized S_{eff} by up to $\approx 70\%$. Moreover, the results show that field-effect passivation on b-Si surfaces works identically to that on planar surfaces when Q_f conditions are high ($|Q_f| > 1 \times 10^{12}$ cm^{-2}), this contradicts the previous hypothesis that a high Q_f will contribute to the minority carrier depletion in b-Si nanofeatures and lead to a boost in surface passivation. Finally, we used the findings of this work to guide how to select the appropriate surface passivation film for b-Si surfaces. For p-type accumulation conditions, a low-Q_f scheme results in a relative improvement when $\sigma_n/\sigma_p < 10$. A moderate-Q_f scheme can result in a significant improvement in surface passivation for high-aspect-ratio b-Si surfaces. A high-Q_f scheme will not show a relative improvement in surface passivation compared with a planar surface; however, these schemes are obviously still preferred as the absolute surface recombination velocities will be the lowest.

Acknowledgment

The authors would like to acknowledge the High Performance Computing service of Katana cluster by the Research Technology Services group at The University of New South Wales. They wouls also like acknowledge the facilities, and the scientific and technical assistance of the Australian National Fabrication Facility–NSW Node and the Australian Microscopy and Microanalysis Research Facility at the Electron Microscope Unit, The University of New South Wales. They would like to thank Y. Zhang, M. U. Khan, Dr. T. H. Fung, and Dr. G. Scardera at the University of New South Wales for characterization assistance and discussion. They would also like to thank the RIE sample support by Rasmus Davidsen at the National Centre for Nanofabrication and Characterization, Technical University of Denmark. The responsibility for the views, information, or advice expressed herein is not accepted by the Australian Government.

References

[1] J. Oh, H.-C. Yuan, and H. M. Branz, "An 18.2%-efficient black-silicon solar cell achieved through control of carrier recombination in nanostructures," *Nat. Nanotechnol.*, vol. 7, no. 11, pp. 743–748, 2012.

[2] H. Savin *et al.*, "Black silicon solar cells with interdigitated back-contacts achieve 22.1% efficiency," *Nat. Nanotechnol.*, vol. 10, no. 7, pp. 624–628, 2015.

[3] X. Liu *et al.*, "Black silicon: Fabrication methods, properties and solar energy applications," *Energy Environ. Sci.*, vol. 7, no. 10, pp. 3223–3263, 2014.

[4] Y. Liu *et al.*, "Nanostructure formation and passivation of large-area black silicon for solar cell applications," *Small*, vol. 8, no. 9, pp. 1392–1397, 2012.

[5] W.-C. Wang *et al.*, "Surface passivation of efficient nanotextured black silicon solar cells using thermal atomic layer deposition," *ACS Appl. Mater. Interfaces*, vol. 5, no. 19, pp. 9752–9759, 2013.

[6] G. von Gastrow *et al.*, "Analysis of the atomic layer deposited Al_2O_3 field-effect passivation in black silicon," *Sol. Energy Mater. Sol. Cells*, vol. 142, pp. 29–33, 2015.

[7] T. H. Fung *et al.*, "Improved emitter performance of RIE black silicon through the application of in-situ oxidation during $POCl_3$ diffusion," *Sol. Energy Mater. Sol. Cells*, vol. 210, 2020, Art. no. 110480.

[8] T. Pasanen, V. Vähänissi, N. Theut, and H. Savin, "Surface passivation of black silicon phosphorus emitters with atomic layer deposited SiO_2/Al_2O_3 stacks," *Energy Proc.*, vol. 124, pp. 307–312, 2017.

[9] V. Naumann, M. Otto, R. B. Wehrspohn, M. Werner, and C. Hagendorf, "Interface and material characterization of thin ALD-Al_2O_3 layers on crystalline silicon," *Energy Proc.*, vol. 27, pp. 312–318, 2012.

[10] P. Repo *et al.*, "Effective passivation of black silicon surfaces by atomic layer deposition," *IEEE J. Photovolt.*, vol. 3, no. 1, pp. 90–94, Jan. 2013.

[11] J. Heinonen, T. P. Pasanen, V. Vähänissi, M. A. Juntunen, and H. Savin, "Modeling field effect in black silicon and its impact on device performance," *IEEE Trans. Electron Devices*, vol. 67, no. 4, pp. 1645–1652, Apr. 2020.

[12] I. T. Heikkinen *et al.*, "AlO_x surface passivation of black silicon by spatial ALD: Stability under light soaking and damp heat exposure," *J. Vac. Sci. Technol. A*, vol. 38, no. 2, 2020, Art. no. 022401.

[13] A. D. Mallorquí *et al.*, "Field-effect passivation on silicon nanowire solar cells," *Nano Res.*, vol. 8, no. 2, pp. 673–681, 2015.

[14] T. Rahman, R. S. Bonilla, A. Nawabjan, P. R. Wilshaw, and S. A. Boden, "Passivation of all-angle black surfaces for silicon solar cells," *Sol. Energy Mater. Sol. Cells*, vol. 160, pp. 444–453, 2017.

[15] D. Turkay, C. Koroglu, and S. Yerci, "Analysis of field-effect passivation in textured and undiffused silicon surfaces," *Phys. Rev. Appl.*, vol. 12, no. 3, 2019, Art. no. 034026.

[16] A. Grove and D. Fitzgerald, "Surface effects on pn junctions: Characteristics of surface space-charge regions under non-equilibrium conditions," *Solid-State Electron.*, vol. 9, no. 8, pp. 783–806, 1966.

[17] A. G. Aberle, S. Glunz, and W. Warta, "Impact of illumination level and oxide parameters on Shockley–Read–Hall recombination at the Si-SiO_2 interface," *J. Appl. Phys.*, vol. 71, no. 9, pp. 4422–4431, 1992.

[18] A. Cuevas *et al.*, "Carrier population control and surface passivation in solar cells," *Sol. Energy Mater. Sol. Cells*, vol. 184, pp. 38–47, 2018.

[19] S. Wang *et al.*, "Understanding field-effect passivation of black silicon: Modeling charge carrier population control in compressed space charge regions," in *Proc. IEEE 47th Photovolt. Spec. Conf.*, 2020, pp. 590–594.

[20] *Sentaurus Device User Guide*, Synopsys, Inc., Mountain View, CA, USA, Version L-2016.03, 2016.

[21] K. R. McIntosh and L. E. Black, "On effective surface recombination parameters," *J. Appl. Phys.*, vol. 116, no. 1, 2014, Art. no. 014503.

[22] S. Olibet, E. Vallat-Sauvain, and C. Ballif, "Model for a-Si:H/c-Si interface recombination based on the amphoteric nature of silicon dangling bonds," *Phys. Rev. B*, vol. 76, no. 3, 2007, Art. no. 035326.

[23] S. Olibet *et al.*, "Properties of interfaces in amorphous/crystalline silicon heterojunctions," *Phys. Status Solidi*, vol. 207, no. 3, pp. 651–656, 2010.

[24] C. Leendertz *et al.*, "Discerning passivation mechanisms at a-Si:H/c-Si interfaces by means of photoconductance measurements," *Appl. Phys. Lett.*, vol. 98, no. 20, 2011, Art. no. 202108.

[25] K. A. Collett *et al.*, "An enhanced alneal process to produce SRV$<$ 1 cm/s in 1 Ω cm n-type Si," *Sol. Energy Mater. Sol. Cells*, vol. 173, pp. 50–58, 2017.

[26] N. E. Grant, T. C. Kho, and K. Weber, "High-level silicon surface passivation by anodically grown silicon dioxide and silicon nitride stacks," *IEEE J. Photovolt.*, vol. 5, no. 4, pp. 1047–1052, 2015.

[27] S. Duttagupta *et al.*, "Dielectric charge tailoring in PECVD SiO_x/SiN_x stacks and application at the rear of Al local back surface field Si wafer solar cells," *IEEE J. Photovolt.*, vol. 5, no. 4, pp. 1014–1019, Jul. 2015.

[28] R. B. Girisch, R. P. Mertens, and R. F. De Keersmaecker, "Determination of Si-SiO_2 interface recombination parameters using a gate-controlled point-junction diode under illumination," *IEEE Trans. Electron Devices*, vol. 35, no. 2, pp. 203–222, Feb. 1988.

[29] Y. Wan, K. R. McIntosh, A. F. Thomson, and A. Cuevas, "Low surface recombination velocity by low-absorption silicon nitride on c-Si," in *Proc. IEEE 38th Photovolt. Spec. Conf.*, 2012, pp. 1–7.

[30] J. Seiffe *et al.*, "Surface passivation of crystalline silicon by plasma-enhanced chemical vapor deposition double layers of silicon-rich silicon oxynitride and silicon nitride," *J. Appl. Phys.*, vol. 109, no. 3, 2011, Art. no. 034105.

[31] M. W. Lamers, K. T. Butler, J. H. Harding, and A. Weeber, "Interface properties of a-SiN_x:H/Si to improve surface passivation," *Sol. Energy Mater. Sol. Cells*, vol. 106, pp. 17–21, 2012.

[32] S. Mack *et al.*, "Silicon surface passivation by thin thermal oxide/PECVD layer stack systems," *IEEE J. Photovolt.*, vol. 1, no. 2, pp. 135–145, Oct. 2011.

[33] R. S. Bonilla, F. Woodcock, and P. R. Wilshaw, "Very low surface recombination velocity in *n*-type c-Si using extrinsic field effect passivation," *J. Appl. Phys.*, vol. 116, no. 5, 2014, Art. no. 054102.

[34] J. Schmidt, F. M. Schuurmans, W. C. Sinke, S. W. Glunz, and A. G. Aberle, "Observation of multiple defect states at silicon–silicon nitride interfaces fabricated by low-frequency plasma-enhanced chemical vapor deposition," *Appl. Phys. Lett.*, vol. 71, no. 2, pp. 252–254, 1997.

[35] J. Schmidt and A. G. Aberle, "Carrier recombination at silicon–silicon nitride interfaces fabricated by plasma-enhanced chemical vapor deposition," *J. Appl. Phys.*, vol. 85, no. 7, pp. 3626–3633, 1999.

[36] A. G. Aberle, "Overview on SiN surface passivation of crystalline silicon solar cells," *Sol. Energy Mater. Sol. Cells*, vol. 65, no. 1–4, pp. 239–248, 2001.

[37] M. Kang *et al.*, "The study of silane-free SiC_xN_y film for crystalline silicon solar cells," *J. Electrochem. Soc.*, vol. 156, no. 6, pp. H495–H499, 2009.

[38] I. Martın *et al.*, "Surface passivation of *p*-type crystalline Si by plasma enhanced chemical vapor deposited amorphous SiC_x:H films," *Appl. Phys. Lett.*, vol. 79, no. 14, pp. 2199–2201, 2001.

[39] I. Martıń *et al.*, "Surface passivation of *n*-type crystalline Si by plasma-enhanced-chemical-vapor-deposited amorphous SiC_x:H and amorphous SiC_xN_y:H films," *Appl. Phys. Lett.*, vol. 81, no. 23, pp. 4461–4463, 2002.

[40] B. Hoex, J. Schmidt, P. Pohl, M. Van de Sanden, and W. Kessels, "Silicon surface passivation by atomic layer deposited Al_2O_3," *J. Appl. Phys.*, vol. 104, no. 4, 2008, Art. no. 044903.

[41] B. Hoex, J. J. H. Gielis, M. C. M. van de Sanden, and W. M. M. Kessels, "On the c-Si surface passivation mechanism by the negative-charge-dielectric Al_2O_3," *J. Appl. Phys.*, vol. 104, no. 11, 2008, Art. no. 113703.

[42] L. E. Black and K. R. McIntosh, "Modeling recombination at the Si–Al_2O_3 interface," *IEEE J. Photovolt.*, vol. 3, no. 3, pp. 936–943, Jul. 2013.

[43] J. Wang, S. S. Mottaghian, and M. F. Baroughi, "Passivation properties of atomic-layer-deposited hafnium and aluminum oxides on Si surfaces," *IEEE Trans. Electron Devices*, vol. 59, no. 2, pp. 342–348, Feb. 2012.

[44] P. Saint-Cast *et al.*, "Variation of the layer thickness to study the electrical property of PECVD Al_2O_3/c-Si interface," in *Proc. Int. Conf. Crystalline Silicon Photovolt.*, Freiburg, Germany, 2011, vol. 8, pp. 642–647.

[45] F. Werner, A. Cosceev, and J. Schmidt, "Interface recombination parameters of atomic-layer-deposited Al_2O_3 on crystalline silicon," *J. Appl. Phys.*, vol. 111, no. 7, 2012, Art. no. 073710.

[46] H. Lee *et al.*, "Surface passivation of crystalline silicon by sputtered AlO_x/AlN_x stacks toward low-cost high-efficiency silicon solar cells," *Jpn. J. Appl. Phys.*, vol. 54, no. 8S1, 2015, Art. no. 08KD18.

[47] G. Krugel *et al.*, "Investigations on the passivation mechanism of AlN:H and AlN:H-SiN:H stacks," *Energy Proc.*, vol. 55, pp. 797–804, 2014.

[48] R. S. Bonilla, K. O. Davis, E. J. Schneller, W. V. Schoenfeld, and P. R. Wilshaw, "Effective antireflection and surface passivation of silicon using a SiO_2/a-TiO_x film stack," *IEEE J. Photovolt.*, vol. 7, no. 6, pp. 1603–1610, Nov. 2017.

[49] K. R. McIntosh *et al.*, "Charge density in atmospheric pressure chemical vapor deposition Tio_2 on SiO_2-passivated silicon," *J. Electrochem. Soc.*, vol. 156, no. 11, pp. G190–G195, 2009.

[50] X. Cheng *et al.*, "Surface passivation properties of HfO_2 thin film on *n*-type crystalline Si," *IEEE J. Photovolt.*, vol. 7, no. 2, pp. 479–485, Mar. 2017.

[51] R. Sreenivasan, P. C. McIntyre, H. Kim, and K. C. Saraswat, "Effect of impurities on the fixed charge of nanoscale HfO_2 films grown by atomic layer deposition," *Appl. Phys. Lett.*, vol. 89, no. 11, 2006, Art. no. 112903.

[52] Y.-K. Chiou, C.-H. Chang, and T.-B. Wu, "Characteristics of hafnium oxide grown on silicon by atomic-layer deposition using tetrakis (ethylmethylamino) hafnium and water vapor as precursors," *J. Mater. Res.*, vol. 22, no. 7, pp. 1899–1906, 2007.

[53] T. G. Allen, M. Ernst, C. Samundsett, and A. Cuevas, "Demonstration of c-Si solar cells with gallium oxide surface passivation and laser-doped gallium p+ regions," in *Proc. IEEE 42nd Photovolt. Spec. Conf.*, 2015, pp. 1–6.

[54] T. G. Allen, Y. Wan, and A. Cuevas, "Silicon surface passivation by gallium oxide capped with silicon nitride," *IEEE J. Photovolt.*, vol. 6, no. 4, pp. 900–905, Jul. 2016.

[55] S. Garud *et al.*, "Surface passivation of CIGS solar cells using gallium oxide," *Phys. Status Solidi*, vol. 215, no. 7, 2018, Art. no. 1700826.

[56] G. Chistiakova, B. Macco, and L. Korte, "Low-temperature atomic layer deposited magnesium oxide as a passivating electron contact for c-Si-based solar cells," *IEEE J. Photovolt.*, vol. 10, no. 2, pp. 398–406, Mar. 2020.

[57] L. E. Black and W. Kessels, "PO_x/Al_2O_3 stacks: Highly effective surface passivation of crystalline silicon with a large positive fixed charge," *Appl. Phys. Lett.*, vol. 112, no. 20, 2018, Art. no. 201603.

[58] L. E. Black and W. E. Kessels, "Investigation of crystalline silicon surface passivation by positively charged PO_x/Al_2O_3 stacks," *Sol. Energy Mater. Sol. Cells*, vol. 185, pp. 385–391, 2018.

[59] Y. Wan, J. Bullock, and A. Cuevas, "Tantalum oxide/silicon nitride: A negatively charged surface passivation stack for silicon solar cells," *Appl. Phys. Lett.*, vol. 106, no. 20, 2015, Art. no. 201601.

[60] Y. Wan, J. Bullock, and A. Cuevas, "Passivation of c-Si surfaces by ALD tantalum oxide capped with PECVD silicon nitride," *Sol. Energy Mater. Sol. Cells*, vol. 142, pp. 42–46, 2015.

[61] B. Macco *et al.*, "Effective passivation of silicon surfaces by ultrathin atomic-layer deposited niobium oxide," *Appl. Phys. Lett.*, vol. 112, no. 24, 2018, Art. no. 242105.

[62] Y. Wan *et al.*, "Zirconium oxide surface passivation of crystalline silicon," *Appl. Phys. Lett.*, vol. 112, no. 20, 2018, Art. no. 201604.

[63] G. Dingemans and W. Kessels, "Status and prospects of Al_2O_3-based surface passivation schemes for silicon solar cells," *J. Vac. Sci. Technol. A*, vol. 30, no. 4, 2012, Art. no. 040802.

[64] P. P. Altermatt, "Models for numerical device simulations of crystalline silicon solar cells—A review," *J. Comput. Electron.*, vol. 10, no. 3, 2011, Art. no. 314.

[65] F.-J. Ma *et al.*, "Advanced modeling of the effective minority carrier lifetime of passivated crystalline silicon wafers," *J. Appl. Phys.*, vol. 112, no. 5, 2012, Art. no. 054508.

[66] M. Ancona and G. Iafrate, "Quantum correction to the equation of state of an electron gas in a semiconductor," *Phys. Rev. B*, vol. 39, no. 13, pp. 9536–9540, 1989.

[67] A. Richter, S. W. Glunz, F. Werner, J. Schmidt, and A. Cuevas, "Improved quantitative description of auger recombination in crystalline silicon," *Phys. Rev. B*, vol. 86, no. 16, 2012, Art. no. 165202.

[68] W. Shockley and W. Read Jr., "Statistics of the recombinations of holes and electrons," *Phys. Rev.*, vol. 87, no. 5, pp. 835–842, 1952.

[69] A. Schenk, "Finite-temperature full random-phase approximation model of band gap narrowing for silicon device simulation," *J. Appl. Phys.*, vol. 84, no. 7, pp. 3684–3695, 1998.

[70] D. Klaassen, "A unified mobility model for device simulation—I. Model equations and concentration dependence," *Solid-State Electron.*, vol. 35, no. 7, pp. 953–959, 1992.

[71] T. Rahman and S. A. Boden, "Optical modeling of black silicon for solar cells using effective index techniques," *IEEE J. Photovolt.*, vol. 7, no. 6, pp. 1556–1562, Nov. 2017.

[72] F. Kersten, A. Schmid, S. Bordihn, J. W. Müller, and J. Heitmann, "Role of annealing conditions on surface passivation properties of ALD Al_2O_3 films," in *Proc. Int. Conf. Crystalline Silicon Photovolt.*, Hamelin, Germany, 2013, vol. 38, pp. 843–848.

[73] M. Wilson, J. Lagowski, L. Jastrzebski, A. Savtchouk, and V. Faifer, "COCOS (corona oxide characterization of semiconductor) non-contact metrology for gate dielectrics," *AIP Conf. Proc.*, vol. 550, no. 1, pp. 220–225, 2001.

[74] R. S. Bonilla, B. Hoex, P. Hamer, and P. R. Wilshaw, "Dielectric surface passivation for silicon solar cells: A review," *Phys. Status Solidi*, vol. 214, no. 7, 2017, Art. no. 1700293.

[75] B. Liao *et al.*, "Excellent c-Si surface passivation by thermal atomic layer deposited aluminum oxide after industrial firing activation," *J. Phys. D, Appl. Phys.*, vol. 46, no. 38, 2013, Art. no. 385102.

[76] B. Hoex, S. Heil, E. Langereis, M. van de Sanden, and W. Kessels, "Ultralow surface recombination of c-Si substrates passivated by plasma-assisted atomic layer deposited Al_2O_3," *Appl. Phys. Lett.*, vol. 89, no. 4, 2006, Art. no. 042112.

[77] R. Khandelwal, U. Plachetka, B. Min, C. Moormann, and H. Kurz, "A comparative study based on optical and electrical performance of micro- and nano-textured surfaces for silicon solar cells," *Microelectron. Eng.*, vol. 111, pp. 220–223, 2013.